



## The impact of weakly bound $^{89}\text{Zr}$ on preclinical studies: Non-specific accumulation in solid tumors and aspergillus infection

Severin, Gregory; Jørgensen, Jesper T.; Wiehr, Stefan ; Rolle, Anna-Maria ; Hansen, Anders Elias; Maurer, Andreas ; Hasenberg, Mike ; Pichler, Bernd ; Kjær, Andreas; Jensen, Andreas Tue Ingemann

*Published in:*  
Nuclear Medicine and Biology

*Link to article, DOI:*  
[10.1016/j.nucmedbio.2014.11.005](https://doi.org/10.1016/j.nucmedbio.2014.11.005)

*Publication date:*  
2015

*Document Version*  
Peer reviewed version

[Link back to DTU Orbit](#)

*Citation (APA):*  
Severin, G., Jørgensen, J. T., Wiehr, S., Rolle, A-M., Hansen, A. E., Maurer, A., Hasenberg, M., Pichler, B., Kjær, A., & Jensen, A. T. I. (2015). The impact of weakly bound  $^{89}\text{Zr}$  on preclinical studies: Non-specific accumulation in solid tumors and aspergillus infection. *Nuclear Medicine and Biology*, 42(4), 360–368. <https://doi.org/10.1016/j.nucmedbio.2014.11.005>

---

### General rights

Copyright and moral rights for the publications made accessible in the public portal are retained by the authors and/or other copyright owners and it is a condition of accessing publications that users recognise and abide by the legal requirements associated with these rights.

- Users may download and print one copy of any publication from the public portal for the purpose of private study or research.
- You may not further distribute the material or use it for any profit-making activity or commercial gain
- You may freely distribute the URL identifying the publication in the public portal

If you believe that this document breaches copyright please contact us providing details, and we will remove access to the work immediately and investigate your claim.

1 **The impact of weakly bound <sup>89</sup>Zr on preclinical studies: Non-specific**  
2 **accumulation in solid tumors and aspergillus infection**

3

4 Gregory W Severin<sup>1,4</sup>, Jesper T Jørgensen<sup>2</sup>, Stefan Wiehr<sup>3</sup>, Anna-Maria Rolle<sup>3</sup>, Anders E  
5 Hansen<sup>2,4,5</sup>, Andreas Maurer<sup>3</sup>, Mike Hasenberg<sup>6</sup>, Bernd Pichler<sup>3</sup>, Andreas Kjær<sup>2</sup>, and Andreas I  
6 Jensen\*<sup>1,4</sup>

7

8 <sup>1</sup> *The Hevesy Laboratory, DTU Nutech, Technical University of Denmark*

9 <sup>2</sup> *Dept. of Clinical Physiology, Nuclear Medicine & PET, Rigshospitalet and Cluster for Molecular*  
10 *Imaging, Faculty of Health Science, University of Copenhagen, Denmark*

11 <sup>3</sup> *Werner Siemens Imaging Center, Department for Preclinical Imaging and Radiopharmacy,*  
12 *Eberhard Karls University Tübingen, Tübingen, Germany*

13 <sup>4</sup> *Center for Nanomedicine and Theranostics, Technical University of Denmark*

14 <sup>5</sup> *Department of Micro- and Nanotechnology, DTU Nanotech, Technical University of Denmark*

15 <sup>6</sup> *University Duisburg-Essen, University Hospital, Institute for Experimental Immunology and*  
16 *Imaging, Essen, Germany;*

17 \* Corresponding author: Technical University of Denmark, Frederiksborgvej 399, bld. 202, 4000

18 Roskilde, Denmark. Tel: +45 20126187; Fax: +45 46775347.

19 E-mail address: [atiije@dtu.dk](mailto:atiije@dtu.dk) (A. Jensen)

20

21 Abbreviated title: <sup>89</sup>Zr accumulation in tumors and aspergillosis

22 Key words: Zr-89, PET/MR, mouse model, cancer, infection, Aspergillus fumigatus

## 23 Abstract

24 Preclinical studies involving  $^{89}\text{Zr}$  often report significant bone accumulation, which is associated  
25 with dissociation of the radiometal from the tracer. However, experiments determining the  
26 uptake of unbound  $^{89}\text{Zr}$  in disease models are not performed as routine controls. The purpose  
27 of the present study was to investigate the impact of free or weakly bound  $^{89}\text{Zr}$  on PET  
28 quantifications in disease models, in order to determine if such control experiments are  
29 warranted. **Methods:** Chemical studies were carried out to find a  $^{89}\text{Zr}$  compound that would  
30 solubilize the  $^{89}\text{Zr}$  as a weak chelate, thus mimicking free or weakly bound  $^{89}\text{Zr}$  released in  
31 circulation.  $^{89}\text{Zr}$  oxalate had the desired characteristics, and was injected into mice bearing  
32 FaDu and HT29 solid tumor xenografts, and mice infected in the lungs with the mold *Aspergillus*  
33 *fumigatus*, as well as in healthy controls (naïve). PET/CT and PET/MR imaging followed to  
34 quantify the distribution of the radionuclide in the disease models. **Results:**  $^{89}\text{Zr}$  oxalate was  
35 found to have a plasma half-life of  $5.1 \pm 2.3$  h, accumulating mainly in the bones of all animals.  
36 Both tumor types accumulated  $^{89}\text{Zr}$  on the order of 2-4% ID/cm<sup>3</sup>, which is comparable to EPR-  
37 mediated accumulation of certain species. In the aspergillosis model, the concentration of  $^{89}\text{Zr}$   
38 in lung tissue of the naïve animals was  $6.0 \pm 1.1$  %ID/g. This was significantly different from that  
39 of the animals with advanced disease, showing  $11.6\% \pm 1.8$  %ID/g. **Conclusions:** Given the high  
40 levels of  $^{89}\text{Zr}$  accumulation in the disease sites in the present study, we recommend control  
41 experiments mapping the biodistribution of free  $^{89}\text{Zr}$  in any preclinical study employing  $^{89}\text{Zr}$   
42 where bone uptake is observed. Aqueous  $^{89}\text{Zr}$  oxalate appears to be a suitable compound for  
43 such studies. This is especially relevant in studies where the tracer accumulation is based upon  
44 passive targeting, such as EPR.

## 45 1. Introduction

46

47  $^{89}\text{Zr}$  is a popular radionuclide for the radiolabeling of monoclonal antibodies (mAbs) and similar  
48 proteins for PET imaging [1–5]. However, several studies on  $^{89}\text{Zr}$ -radiolabeled mAbs show  
49 significant bone uptake of  $^{89}\text{Zr}$  [2,6,7]. This uptake is often attributed to chelate instability, with  
50  $^{89}\text{Zr}$  being released during the long circulation time of the mAb [2]. Alternatively, Holland et al.  
51 suggested a metabolic process [8]. Regardless of the cause, the accumulation of radioactivity in  
52 bones is indicative of  $^{89}\text{Zr}$  that is no longer bound to the tracer. The presence of this unbound  
53  $^{89}\text{Zr}$  during a PET scan can potentially have a large impact on the interpretation of results,  
54 especially if it is accumulating at the disease site. In current practice however, appropriate  
55 control experiments are not reported.

56

57 The biodistribution of free, or weakly chelated,  $^{89}\text{Zr}$  was investigated in healthy mice by Abou et  
58 al. using the chloride, oxalate, phosphate and citrate salts [9]. All salts were found to exhibit  
59 similar biodistribution and cause accumulation of  $^{89}\text{Zr}$  in the bones, except the phosphate,  
60 which localized to liver and spleen. This was attributed to poor solubility of the  $^{89}\text{Zr}$  phosphate.  
61 Holland et al. also found the activity from the  $^{89}\text{Zr}$  oxalate to show pronounced bone  
62 accumulation, but found  $^{89}\text{Zr}$  injected as the chloride to accumulate in the liver [8]. This was  
63 also attributed to the chloride being prone to hydrolysis and poor solubility. These studies both  
64 indicated that free, soluble  $^{89}\text{Zr}^{4+}$  will accumulate in bone.

65

66 The nonspecific biodistribution of free  $^{89}\text{Zr}$  in clinically relevant disease models has not been  
67 investigated. However, given the large number of reports showing increased bone uptake in  
68 monoclonal antibody imaging, which indicates the presence of free  $^{89}\text{Zr}$ , knowledge of the  
69 distribution of free  $^{89}\text{Zr}$  in animal models of human disease is important. In tumors, the  
70 accumulation of naked or weakly chelated radiometals, such as  $^{67}\text{Ga}$  [10], and  $^{64}\text{Cu}$  [11], is well  
71 established. For this reason,  $^{67}\text{Ga}$  salts have a long history of use in tumor imaging.  $^{67}\text{Ga}$   
72 distributes via binding to transferrin [10], and it is reasonable to suspect that the same pathway  
73 might be available for  $\text{Zr}^{4+}$ , or  $\text{ZrO}^{2+}$  [12]. Accordingly, free  $^{89}\text{Zr}$  could show nonspecific tumor  
74 accumulation through this pathway, which might disturb the correct interpretation of  
75 accumulation data from mAb imaging. In addition, enhanced permeation and retention (EPR)  
76 dominated localization after metal association with endogenous serum proteins, such as  
77 albumin, may give rise to lesion uptake of free  $^{89}\text{Zr}$  [13,14]. As nanoparticles are typically  
78 thought to localize to tumors via EPR [15], the presence of free  $^{89}\text{Zr}$  may have consequences for  
79 the interpretation of tumor accumulation data for  $^{89}\text{Zr}$ -labeled nanoparticles.

80

81  $^{89}\text{Zr}$ -labeled antibodies are not only in use for tumor imaging, but are also being investigated for  
82 the diagnosis of other diseases such as pulmonary aspergillosis. In *Aspergillus fumigatus*  
83 infections, an extracellular siderophore is excreted by the mold [16]. This was recently utilized  
84 by Petrik et al. in preclinical PET studies with  $^{68}\text{Ga}$  labeled siderophores TAFC and FSC [17,18].  
85 These chelators exhibit multiple hydroxamate groups, similar to the most successful  $^{89}\text{Zr}$   
86 chelator desferrioxamine B, which itself is a siderophore produced by streptomyces bacteria  
87 [19]. Such extracellular siderophores may take up free or weakly bound  $^{89}\text{Zr}$  and facilitate its

88 accumulation in *Aspergillus* infected tissues. This accumulation, coupled with the EPR-mediated  
89 accumulation occurring as a result of inflammation and transferrin-receptor upregulation, could  
90 give a very significant PET signal from lung accumulation of free or weakly bound  $^{89}\text{Zr}$  in  
91 circulation in pulmonary aspergillosis. Therefore, knowledge of the biodistribution of free  $^{89}\text{Zr}$   
92 in solid tumors as well as in other disease sites, such as *A. fumigatus* infected tissues, is crucial  
93 before initiating a preclinical positron emission tomography (PET) study with  $^{89}\text{Zr}$ .

94

95 The aim of this work was to investigate the biodistribution of weakly chelated  $^{89}\text{Zr}$  in relevant  
96 murine disease models compared to their healthy controls. We set out to determine whether 1)  
97 free  $^{89}\text{Zr}$  exhibits accumulation in FaDu and HT29 tumor xenografts in mice and 2) whether  
98 biodistribution, especially in lungs, is significantly different between healthy animals and those  
99 with pulmonary aspergillosis. Further, the criteria for the injected  $^{89}\text{Zr}$  to be considered 'free',  
100 was that it was stable in solution and able to interact and associate with complexing molecules  
101 and other blood stream components. For this reason we also investigated a range of  
102 complexing ligands for their ability to restrict hydrolysis of  $^{89}\text{Zr}$  and allow chelation by  
103 *diethylene triamine pentaacetic acid* (DTPA).

104

## 105 2. Materials and Methods

106

### 107 2.1. Materials

108 Yttrium foils were purchased from Alfa Aesar. All solvents and chemicals were purchased from  
109 Sigma Aldrich.  $^{89}\text{Zr}$  was produced on a GE PETtrace Cyclotron. Radio-TLC was performed on a  
110 Raytest MiniGita Star. All TLC analyses were performed on silica gel 60 F<sub>254</sub> plates (Merck) with  
111 5% (w/v) NH<sub>4</sub>OAc in H<sub>2</sub>O-MeOH (1:1) as eluent, in which the R<sub>f</sub> of  $^{89}\text{Zr}$ -DTPA is 0.7 and  $^{89}\text{Zr}^{4+}$   
112 does not elute. Radioactivity was measured using a Veenstra Instruments dose calibrator VDC-  
113 505. QMA cartridges were from Waters. Osmolalities were measured on an Osmomat 030  
114 cryoscopic osmometer (Gonotec). pH was measured on an Inolab 740 electronic pH-meter  
115 (WTW). Radionuclidic purity was measured on an LGC-5 high purity germanium detector  
116 (Princeton Gamma-Tech). Metal ions were quantified with an ICAP 7000 ICP-OES (Thermo  
117 Scientific). Ultrapure water was used in all cases (Milli-Q water purification system, Millipore).

118

119  $^{89}\text{Zr}$  chloride was prepared according to the method of Holland *et al.* [20]. In brief, natural 660  
120  $\mu\text{m}$  thick yttrium foils, were irradiated with 15  $\mu\text{A}$  of protons degraded from 16 MeV to 11 MeV  
121 with an 800  $\mu\text{m}$  aluminum plate. The produced  $^{89}\text{Zr}^{4+}$  was separated from the yttrium target  
122 after digestion in aqueous HCl (3 mL, 6 M) by trapping on hydroxamate resin (50-100 mg),  
123 followed by elution of the  $^{89}\text{Zr}^{4+}$  in aqueous oxalic acid (3 mL, 1 M). A quarternary methyl  
124 ammonium Sep-Pak cartridge (QMA light, Waters) was used to trap the anionic  $^{89}\text{Zr}$  oxalate  
125 complex from the oxalic acid solution, and after washing with ultrapure water (30 mL), the  $^{89}\text{Zr}$

126 was released in aqueous HCl (200  $\mu$ L, 2 M). This solution was taken to dryness under argon flow  
127 at 110  $^{\circ}$ C for 15 minutes, furnishing  $^{89}\text{Zr}$  chloride.

128

## 129 **2.2. Comparison of aqueous solutions for injection of 'free' $^{89}\text{Zr}$**

130 The following experiments were performed to test the ability of various complexing ligands to  
131 restrict hydrolysis of  $^{89}\text{Zr}$  and allow chelation by DTPA. To vials containing dry  $^{89}\text{Zr}$  chloride was  
132 added 1.3 mL of either 1) saline, 2) 10 mM oxalic acid in saline at pH  $\approx$  5.5, 3) 10 mM oxalic acid  
133 in saline at pH  $\approx$  7.0, 4) 10 mM citric acid in saline at pH 5.5, 5) 10 mM citric acid in saline at pH  
134 7.0, 6) neat ultrapure water, 7) isotonic sucrose solution at 924 mg/mL, 8) 10 mM sodium  
135 acetate at pH 5.5 or 9) 10 mM sodium acetate at pH  $\approx$  7.0. Each preparation was stirred for 10  
136 minutes at 37  $^{\circ}$ C after which 300  $\mu$ L was removed for pH measurement. In addition, the  
137 radioactivity in the total volume (1.3 mL) as well as in the removed 300  $\mu$ L was measured. To  
138 the remaining 1.00 mL was then added aqueous DTPA (50  $\mu$ L, 50 mM) that had been adjusted  
139 to pH 5.5 or pH 7.0, whichever was closest to the pH of the receiving  $^{89}\text{Zr}$ -mixture. To the saline  
140 (chloride), water and sucrose mixtures was added DTPA at pH 5.5. The solutions were then  
141 stirred at 37  $^{\circ}$ C and monitored by radio-TLC with samples removed at t = 0 (before addition of  
142 DTPA), t = 10 min, t = 30 min and t = 60 min. Each mixture was prepared and analyzed in  
143 triplicate.

144

## 145 **2.3 Preparation and characterization of the $^{89}\text{Zr}$ oxalate for *in vivo* use**

146 Based on the stability and exchange experiments described above, an oxalate solution was  
147 chosen for *in vivo* use. This was prepared by adding a solution of 10 mM oxalic acid in isotonic



148 saline (pH adjusted to 6.7 with NaOH) to the dried  $^{89}\text{Zr}$  chloride. In order to confirm that the  
149  $^{89}\text{Zr}$  was fully dissolved, a sample of the solution was removed and its activity concentration  
150 was compared to the remaining fraction. Osmolality and pH were measured, and HPGE gamma  
151 spectroscopy was used to determine the radionuclidic purity. ICP-OES, calibrated against Fe, Zr,  
152 Zn, Cu, Ag, and Ni standards in 1% (w/v) HCl, was used to quantify metal impurities.  
153 Additionally, 300  $\mu\text{l}$  of the  $^{89}\text{Zr}$  oxalate solution was removed and mixed with aqueous DTPA (15  
154  $\mu\text{L}$ , 50mM, pH 7.0). After stirring at 37 °C for 30 min, it was analyzed by radio-TLC along with a  
155 sample to which no DTPA had been added. After the completion of these tests, the solution  
156 was ready for injection in the animal studies.

157

#### 158 ***2.4 In vivo studies on tumor-bearing mice***

159 The studies on tumor-bearing mice were approved by the Danish Animal Welfare Council,  
160 Ministry of Justice. Human head and neck cancer cell line, FaDu and human colorectal cancer  
161 cell line, HT29 (purchased from ATCC) were cultured in MEM medium with Earle's salts and  
162 McCoy's 5A medium, respectively (both from Sigma-Aldrich); with 10% fetal calf serum, and  
163 100 units/mL penicillin and 100  $\mu\text{g}/\text{mL}$  streptomycin (Invitrogen) at 37 °C in 5%  $\text{CO}_2$ . In addition  
164 the MEM medium was supplemented with 1% MEM non-essential amino acids solution (100x),  
165 1 mM sodium pyruvate (both from Invitrogen) and 2 mM L-glutamine (Sigma-Aldrich). Tumors  
166 were established in the left and right flank of seven-week old female NMRI nude mice (Taconic  
167 Europe) by subcutaneous injection of  $10^6$  cancer cells dissolved in 200  $\mu\text{L}$  of a 1:1 mixture of  
168 Matrigel<sup>TM</sup> (BD-Biosciences) and growth medium and were allowed to grow for 2-3 weeks for  
169 tumor volumes of 50-500  $\text{mm}^3$ . Animals had access to chow and water ad libitum. For tracer

170 administration and during scans, the mice were placed in a nose cone and breathed gas  
171 anesthesia (2.5% Sevoflurane (Abbot Scandinavia) mixed with 35% O<sub>2</sub> in N<sub>2</sub>). A heating pad was  
172 used to keep the body temperature stable. <sup>89</sup>Zr oxalate solution (100 μL, 9-15 MBq) was  
173 injected into the tail vein of mice bearing FaDu (n = 3) and HT29 tumor xenografts (n = 4). Ten  
174 minute static scans were performed on a small animal PET scanner (microPET 120, Siemens  
175 Medical Solutions) at 1 h, 6 h, 20 h, 45 h, and 68 h post injection with an energy window 350-  
176 650 keV and 6 ns time resolution. Each PET scan was followed by seven minutes small animal CT  
177 scans (MicroCAT II Tomograph; Siemens Medical Solutions) with tube voltage and tube current  
178 set at 70 kVp and 500 μA, respectively and an exposure time of 310 ms per projection (360°;  
179 360 projections). Listmode data from PET acquisitions were post-processed into sinograms and  
180 reconstructed using the maximum a posteriori (MAP) algorithm. Images had a resolution of 1.2  
181 mm at the center field of view. PET and CT images were fused using Inveon software (Siemens  
182 Medical Solutions), ROIs were drawn on different target tissue and uptake quantified as %  
183 injected dose per cubic centimeter (%ID/cm<sup>3</sup>). Additionally, the tumor-to-muscle (T/M) and  
184 tumor-to-blood (T/B) ratios were calculated. From the images it was evident that the  
185 myocardium did not accumulate high levels of <sup>89</sup>Zr oxalate. As it is impossible to delineate the  
186 left ventricle of the mice based on CT scans without contrast, a ROI created on the heart was  
187 used for T/B-ratio and blood-circulation half-life calculations.

188

### 189 ***2.5 In vivo studies on A. fumigatus infected and naïve mice***

190 The studies on *A. fumigatus* infected and disease-free control mice (“naïve”) were performed  
191 according to the German Animal Protection Law with permission from the responsible local

192 authorities. Infections were performed as described by Bruns *et al* [21]. Briefly, eight-week old  
193 female C57BL/6 mice (Harlan Laboratories) were rendered neutropenic by an intraperitoneal  
194 injection of 100  $\mu$ L anti-Gr-1 antibody solution (clone RB6-8C5 at a concentration of 1 mg/mL,  
195 BioXCell). 24 h later a pulmonary *A. fumigatus* infection was induced by an intratracheal  
196 application of  $4 \times 10^6$  resting *A. fumigatus* spores (strain ATCC 46645), suspended in 100  $\mu$ L  
197 sterile tap water. For this step the animals were anaesthetized by an intraperitoneal injection of  
198 100  $\mu$ L Ketamin/Rompun solution (Ketamin: 80 mg/kg, Ratiopharm GmbH, Ulm, Germany;  
199 Rompun: 15 mg/kg, Bayer HealthCare, Leverkusen, Germany). After reaching deep narcosis, the  
200 animals were intubated using a 22G indwelling venous catheter (Vasofix Braunüle, B. Braun AG,  
201 Melsungen, Germany) and subsequently the spore suspension was applied. To achieve a better  
202 distribution of the spore mass and to avoid suffocation the animals were ventilated for one  
203 minute with a small animal respirator (MiniVent, Hugo Sachs, March-Hugstetten, Germany) at a  
204 rate of 250 breaths per minute at an inhalation volume of 300  $\mu$ L per breath. Animals had  
205 access to food and water ad libitum.

206  
207  $^{89}\text{Zr}$  oxalate solution (50  $\mu$ L, 10-12 MBq), was injected via the lateral tail vein. During imaging,  
208 the animals were anesthetized with 1.5% isoflurane mixed with 100% oxygen. Anesthesia was  
209 monitored by measuring the respiratory frequency, and the body temperature was kept at 37°C  
210 by a heating pad. All mice were imaged using a small animal PET scanner (Inveon, Siemens  
211 Preclinical Solutions), yielding a spatial resolution of approximately 1.3 mm. PET data were  
212 acquired in list-mode, histogrammed in one 10 min time frame for the static scans and  
213 reconstructed using an iterative ordered subset expectation maximization (OSEM) algorithm.

214 No attenuation correction was applied. Magnetic resonance (MR) imaging was performed on a  
215 7 T small animal MR tomograph (Clinscan, Bruker Biospin MRI) obtaining anatomical  
216 information for optimized organ delineation. A T2-weighted 3D space sequence (TE / TR 202 /  
217 2500 ms, image matrix of 137 x 320, slice thickness 0.27 mm) was used for whole-body imaging.  
218 PET images were normalized to each other, subsequently fused to the respective MR images  
219 and analyzed using Inveon Research Workplace software (Siemens Preclinical Solutions).  
220 Results are expressed as percentage of the injected dose per cm<sup>3</sup> (%ID/cm<sup>3</sup>). After the last PET  
221 scan, the animals were sacrificed by cervical dislocation under deep anesthesia and dissected.  
222 Organs were removed, weighed and measured with an aliquot of injected solution in the  $\gamma$ -  
223 counter (Wizard single-detector  $\gamma$ -counter; Perkin Elmer) using an energy window between 350  
224 and 650 keV.

225  
226 The *A. fumigatus* infected mice were divided into two different groups. The first group (n = 5),  
227 termed “nascent disease”, received the tracer injection immediately after infection. These  
228 animals, along with neutropenic uninfected controls (n = 5), “naïve”, mice were imaged with 10  
229 min PET scans, followed by MR imaging, performed at 3, 24 and 48 h post-injection of the  
230 tracers. In the second group (n = 4), termed “advanced disease”, infected mice were injected  
231 with <sup>89</sup>Zr oxalate 21 hours after infection. This cohort, along with four naïve control animals,  
232 was imaged 3 h after tracer injection, followed immediately by *ex vivo* biodistribution.

233

## 234 **2.6 Statistical Analysis**

235 Statistical analysis was performed using a two-tailed t-test. Data were considered statistically  
236 significant for  $p < 0.05$ . All quantitative results are shown as the mean  $\pm$  1 standard deviation  
237 (SD).

238

## 239 **3. Results**

240

### 241 **3.1 Comparison of aqueous solutions for injection of 'free' <sup>89</sup>Zr**

242 The results from the tests on the various <sup>89</sup>Zr-mixtures are presented in **table 1** (pH values for  
243 the mixtures) and **figures 1A** (transferability/dissolution) and **1B** (transchelation to DTPA). For  
244 the pH measurements in general, the solutions with low buffer capacity at their respective pH  
245 values became slightly more acidic after mixing with the dried <sup>89</sup>Zr activity. This was likely due  
246 to leftover oxalic acid residue from the chemical separation. Our lowest water pH measurement  
247 was pH = 4.65, which indicates that oxalic acid concentration was less than 13 μM (see  
248 **supplemental materials** for calculation). According to the work of Kobayashi *et al.* [22], Zr<sup>4+</sup> is  
249 present as the insoluble hydroxide complex at such low oxalate concentrations. This was  
250 reflected by our transferability tests (**figure 1A**). In solutions with an efficient complexing agent  
251 in sufficient concentration to restrict hydrolysis, such as oxalate, citrate, or sucrose, <sup>89</sup>Zr was  
252 readily taken into the aqueous phase, whereas hydrolysis-prone mixtures, such as water,  
253 acetate, and chloride, resulted in incomplete dissolution of the <sup>89</sup>Zr.

254

255 Despite the fact that several solutions were able to bring <sup>89</sup>Zr into the aqueous environment, it  
256 remained necessary to test whether the <sup>89</sup>Zr was still able to transchelate to DTPA. This would  
257 ensure that the <sup>89</sup>Zr was not merely suspended as a colloid, and that the complexes in question  
258 could easily transfer the radioactivity to other agents. All complexes were tested for  
259 transchelation to DTPA, but only the ones with superior transferability are shown in **figure 1B**.  
260 For the remainder, please refer to **supplemental materials**. Both oxalate mixtures showed fast

261 and efficient transchelation to DTPA, within 10 minutes. On the other hand, the uptake from  
262 the citrate was markedly slower, showing a gradual ascent, reaching about 70-80% after one  
263 hour. DTPA chelation from the sucrose was faster than from the citrate, but slower than from  
264 the oxalate.

265  
266 Based on the results described above, we decided to use the oxalate complex for *in vivo*  
267 studies, while keeping the pH below 7. The main reason for choosing oxalate over citrate was  
268 that we desired a complex with a higher propensity for transferring  $^{89}\text{Zr}$  to other chelating  
269 agents present in serum. This was expected to prevent fast renal clearance of the charged  
270 complexes and to better mirror the *in vivo* situation where weakly bound  $^{89}\text{Zr}$  is released and  
271 presumably bound to endogenous serum components.

272  
273 ***3.2 Preparation and characterization of the  $^{89}\text{Zr}$  oxalate solution for *in vivo* use***

274 The results of the quality control analyses for the injected  $^{89}\text{Zr}$  oxalate solutions were consistent  
275 with those observed in the transferability/solubility and transchelation tests described above.  
276 The transferability of activity in the  $^{89}\text{Zr}$  oxalate *in vivo* formulation was 95%, indicating that the  
277  $^{89}\text{Zr}$  was properly dissolved. The pH value was in the range of 5.5-6.7, which due to the low  
278 buffer capacity of the solution was expected to fluctuate. The osmolality was 310 mOsmol/kg,  
279 and was appropriate for injection (serum osmolality: 282 - 295 mOsmol/kg). Analysis by ICP-  
280 OES showed both non-radioactive Zr and Fe to each be present in concentrations on the order  
281 of 200 ppb. This gave specific activities against total Zr and Fe of 20-35 GBq/ $\mu\text{mol}$  at time of  
282 injection. Analysis by gamma spectroscopy showed only peaks originating from  $^{89}\text{Zr}$ , indicating

283 radionuclidic purity over 99%. Analysis of the  $^{89}\text{Zr}$  oxalate solution by radio-TLC showed that  
284 >99% of the activity stayed at the origin. Following addition of DTPA, 98% of the activity shifted  
285 to the Zr-DTPA peak after 30 minutes (93% after 10 minutes). This confirmed a radiochemical  
286 purity of >95%, and that the activity was freely transchelated from the oxalate complex to other  
287 chemical species.

288

### 289 **3.3 In vivo data from tumor-bearing mice**

290 Representative PET/CT images from the FaDu and HT29 tumor-bearing animals are given in  
291 **Figure 2**, with organs denoted. Tumor contrast is clearly seen at both 1 h and 45 h. However, 45  
292 h images are dominated by high bone accumulation.

293

294 Quantifications of the PET data are given in **Table 2**. Both tumor types showed significant  
295 uptake of 2-4% ID/cm<sup>3</sup> over the course of the study. As expected, bone uptake was prominent,  
296 reaching a maximum at 20 h, followed by a plateau at around 13% ID/cm<sup>3</sup>. The tumor-to-  
297 muscle (T/M) and tumor-to-blood (T/B) ratios in each tumor model are displayed in **Figure 3**.  
298 The T/M values ranged from 1.5-3.7 at all time-points, reflecting the contrast observed in  
299 **Figure 2**. The long circulation time of the  $^{89}\text{Zr}$  oxalate is evident in the heart ROI data. To obtain  
300 the clearance half-life, the heart ROI time activity curve for each animal was fitted with an  
301 exponential function (unweighted least squares fit with constant background). The average ( $\pm 1$   
302 SD) blood clearance half-life was  $5.1 \pm 2.3$  h ( $n = 7$ ) (refer to **supplemental materials** for  
303 calculation).

304



305 **3.4 In vivo data from *Aspergillus*-infected mice and healthy controls**

306 The mice infected with *A. fumigatus* were divided into two groups. In the nascent disease  
307 group, where animals received the tracer injection immediately after they had been infected,  
308 and their naïve controls, the PET and biodistribution data were independent of disease status  
309 **(Figure 4A-D)**. Quantification of the PET results revealed enhanced uptake of  $^{89}\text{Zr}$  in the spine  
310 **(Figure 4C)** without significant differences between the tested groups. The bone uptake pattern  
311 is evident by qualitative observation in the 48 h maximum intensity projection (MIP) images in  
312 **Figure 4E**. The mean tracer uptake in the spine of naïve mice increased from  $7.5 \pm 0.9 \text{ \%ID/cm}^3$   
313 at 3 h to  $18.6 \pm 1.0 \text{ \%ID/cm}^3$  at 24 h, and in infected animals from  $7.5 \pm 0.3 \text{ \%ID/cm}^3$  at 3 h to  
314  $16.5 \pm 1.6 \text{ \%ID/cm}^3$  at 24 h after tracer injection, further reflecting the similarity between  
315 infected and naïve animals.

316  
317 Contrastingly, for the group of animals with advanced disease, those infected with *A. fumigatus*  
318 21 hours prior to tracer injection, the biodistributions were markedly different from the healthy  
319 controls. Static PET images at 3 hours post injection **(Figure 5)** revealed significantly higher  
320 uptake of  $^{89}\text{Zr}$  ( $7.8 \pm 1.3 \text{ \%ID/cm}^3$ ) in the lungs of *A. fumigatus* infected animals compared to the  
321 naïve group ( $5.7 \pm 0.3 \text{ \%ID/cm}^3$ ;  $p = 0.048$ , **Figure 6**) In addition, the uptake of  $^{89}\text{Zr}$  in the spine  
322 of naïve animals was significantly higher ( $6.5 \pm 0.7 \text{ \%ID/cm}^3$ ) compared to the infected group  
323 ( $4.8 \pm 0.3 \text{ \%ID/cm}^3$ ;  $p = 0.0088$ , **Figure 6**). No significant differences were seen in liver and  
324 muscle tissues **(Figure 6)**.

325

326

327 The *ex vivo* biodistribution from the advanced disease group confirmed the quantification  
328 obtained from the PET imaging (**Table 3**). The data from all animals revealed high  
329 concentrations of <sup>89</sup>Zr in the bones, blood, and highly blood-perfused organs such as the heart.  
330 The %ID/g values of the blood were 10.5 ± 2.7 (naïve animals) and 8.6 ± 2.8 (advanced disease).  
331 The *ex vivo* biodistribution confirmed the significant differences in the lung (p = 0.002) and  
332 spine (p = 0.045) uptake between the infected and naïve animals observed with *in vivo* PET  
333 quantification.

334

335

336

337

338

339

340

341

342

343

344

345

346

## 347 **4 Discussion**

348

349  $^{89}\text{Zr}$  has a half-life of 3.27 days and is therefore a useful radionuclide for elucidating the  
350 biodistribution of long-circulating, biologically relevant molecules, such as antibodies and  
351 nanoparticles. Currently, it is one of the most widely used nuclides for PET imaging at time-  
352 points beyond two days post-injection. It allows researchers to understand how a labeled  
353 molecule distributes, giving useful information that leads to better drug and tracer  
354 development.

355

356 The weakness in the current practice is that the derived images quantify the distribution of the  
357 radionuclide and not necessarily the intact tracer. In general this is a well-understood  
358 phenomenon in PET that can be controlled for by metabolite analysis. However, in  $^{89}\text{Zr}$  imaging  
359 the problem is rarely addressed. This is surprising because in a large number of pre-clinical  
360 studies involving  $^{89}\text{Zr}$  there is heightened bone accumulation in the animals. Such high skeletal  
361 uptake is indicative of  $^{89}\text{Zr}$  that is no longer bound to the molecule of interest, but is free or  
362 weakly coordinated. Given that there is an observed separation between radionuclide and the  
363 traced molecule, it is important to understand how the free radionuclide is affecting the PET  
364 data.

365

366 In PET imaging of antibodies  $^{89}\text{Zr}$  is usually located in the desferrioxamine (Df) chelator. Within  
367 Df, it is present as  $^{89}\text{Zr}^{4+}$ , with water taking up the remaining coordination sites rather than =O  
368 or -OH [8]. This incomplete occupation of the first coordination shell by Df has been pointed to

369 as a chink in the armor of an otherwise incredibly stable chelate, and a possible cause for  
370 release of free  $^{89}\text{Zr}$  in preclinical studies [23]. Another reason for the presence of free  $^{89}\text{Zr}$  in  
371 mAb studies is non-specific binding of the radiometal to the protein. Often, radiolabeling is  
372 reported with less than 100% yield [6,7], which means either that Df-chelation sites were in  
373 shortage or that the reaction had not run to completion. In such cases surplus  $^{89}\text{Zr}$  will be  
374 present in the reaction mixture and it is reasonable to assume that some of it could bind non-  
375 specifically to certain proteins. Finally, it is possible that free  $^{89}\text{Zr}$  arises from metabolism of the  
376 radiolabeled entities.

377  
378 Regardless of the mechanism by which  $^{89}\text{Zr}$  is released to the circulation, we sought a tracer  
379 that would solubilize and efficiently disperse the  $^{89}\text{Zr}$  while restricting irreversible hydrolysis.  
380 We found that a solution of the radioactivity in 10 mM oxalate in isotonic saline with a pH of  
381 5.0-6.5 adequately provided the desired properties. This was shown by the high solubility of the  
382  $^{89}\text{Zr}$  in the mixture and its rapid chelation by DTPA. In addition, the *in vivo* results showed  
383 limited liver accumulation. This is consistent with results reported by Abou et al. and by Holland  
384 et al. where  $^{89}\text{Zr}$  oxalate was not accumulating in the liver of healthy animals [8,9]. On this  
385 basis, we conclude that our injected  $^{89}\text{Zr}$  was adequately dissolved. Also, the plasma half-life of  
386 our injected activity was  $5.1 \pm 2.3$  h. Usually, small molecular, exogenous, highly charged  
387 species, such as  $^{89}\text{Zr}$  oxalate, can be expected to undergo fast renal clearance, as is the case  
388 with free  $^{89}\text{Zr}$ -Df [8]. For this very reason, the short circulation time of  $^{89}\text{Zr}$ -Df makes it unsuited  
389 as a tracer for monitoring the biodistribution of weakly bound  $^{89}\text{Zr}$ . That the injected  
390 radioactivity in our studies showed prolonged retention in blood suggests that either the

391 activity is shifted to other endogenous carriers with long circulation, or that the  $^{89}\text{Zr}$  oxalate  
392 itself is long-circulating. In both cases, since the oxalate is a weak complex, the long circulatory  
393 property of the activity is beneficial to its distribution *via* the routes that could be expected of  
394  $^{89}\text{Zr}$  weakly bound to long-circulating species, such as antibodies or nanoparticles.

395  
396 Our initial screening of  $^{89}\text{Zr}$  formulations revealed chloride (as saline) to inadequately prevent  
397 hydrolysis and keep  $^{89}\text{Zr}$  in solution, for which reason we deemed it unfit for *in vivo* use without  
398 an additional complexing ion. This agreed with the studies performed by Holland et al., where  
399 the chloride formulation was found to exhibit heavy liver accumulation [8]. In contrast, Abou et  
400 al. found the chloride (as saline) to distribute similarly to otherwise free  $^{89}\text{Zr}$ , with activity  
401 mainly localizing to bones [9]. Accordingly, there is a discrepancy between the results of these  
402 groups with regards to the chloride. Our study primarily supports the results for the chloride  
403 achieved by Holland et al. It is possible that traces of oxalic acid remaining after preparation of  
404 the chloride could aid in the solubilization and unrestricted biodistribution of  $^{89}\text{Zr}$  present in an  
405 otherwise chloride containing mixture. It should be noted that we employed the same method  
406 for preparing the  $^{89}\text{Zr}$  chloride as Holland et al., and therefore we could be expected to observe  
407 the same insolubility [8].

408  
409  $^{89}\text{Zr}$  that is released *in vivo* has the opportunity of being taken up by endogenous binding  
410 agents. Likely candidates for such binding include transferrin (Tf) and albumin. Transferrin  
411 labeled with  $^{89}\text{Zr}$  through Df has been shown to accumulate in tumors and inflammations, due  
412 to the upregulation of transferrin receptors as part of an inflammatory response [24,25].

413 However, binding of  $^{89}\text{Zr}$  to the endogenous ferric binding site of transferrin without the use of  
414 a chelator was found to be less suitable for *in vivo* use by Holland *et al.* [24]. The conclusion  
415 that endogenous labeling was not viable as a method for producing stable  $^{89}\text{Zr-Tf}$  for *in vivo*  
416 imaging does not exclude the possibility of *in vivo*  $^{89}\text{Zr}$  transport via transferrin. The somewhat  
417 analogous labeling of transferrin by  $^{45}\text{Ti}$ , and its subsequent reported localization to tumors,  
418 indicates that tumor accumulation of hard, oxophilic radiometals can be due to binding to  
419 transferrin [26]. The results from the HT29 and FaDu tumor models presented here do not  
420 show the striking contrast (14.9 %ID/cm<sup>3</sup> tumor accumulation at 24 h) observed by Vavere *et al.*  
421 for  $^{45}\text{Ti}$ -transferrin; albeit the difference could be attributed to the different affinities of  
422 transferrin toward the metals. However, the range of the tumor accumulations we observed  
423 are consistent with uptake based upon EPR, such as that of radiolabeled nanoparticles, which is  
424 usually in the range of 3-6 %ID/cm<sup>3</sup> [27–29]. Albumin may be a vehicle for tumor accumulation  
425 of certain species such as radiometals or their hydroxides/oxides due to its metal binding  
426 capabilities [13]. Albumin has been labeled with  $^{89}\text{Zr}$  through desferrioxamine and gave a  
427 biodistribution in tumor-bearing animals that was dominated by EPR-mediated tumor  
428 accumulation, with tumor values of 2-5 %ID/cm<sup>3</sup> measured until 20 h post injection [14]. While  
429 the level of tumor accumulation (2-4% ID/cm<sup>3</sup>) observed in the present study is negligible with  
430 respect to signals observed with many highly specific mAbs (*eg.* J591-PSMA in LnCaP  
431 xenografts, 34-46 %ID/cm<sup>3</sup>, [8]), it is not small compared to the uptakes expected in non-  
432 targeted nanoparticle imaging. Therefore, as  $^{89}\text{Zr}$  becomes more prevalent in nanoparticle  
433 imaging, differentiating between the non-specific accumulation of free  $^{89}\text{Zr}$ , versus that of the  
434 nanoparticles, must be taken into account.

435

436 As a further point, it should be noted that the impact of non-specific accumulation of free  $^{89}\text{Zr}$   
437 in spontaneous human cancers is unknown. If free  $^{89}\text{Zr}$  exhibits tumor accumulation due to the  
438 EPR effect, translation from mice to humans may amplify the significance of non-specific  
439 uptake, especially in the case of imaging with  $^{89}\text{Zr}$ -labeled mAbs. When imaging EPR-localizing  
440 agents, an increased tumor accumulation relative to total body mass from mice to humans is  
441 typically seen. Harrington et al. investigated  $^{111}\text{In}$ -labeled liposomes and found tumor uptakes  
442 in mice ranging from 1-6 %ID/g over several days post-injection in an HNSCC-derived xenograft  
443 model [30]. In humans, they found a tumor uptake of  $33 \pm 16$  %ID/kg at 72 hours [31]. On the  
444 contrary, targeted mAb imaging with U36 against HNX-OE (HNSCC-derived) xenografts in mice  
445 gave a striking uptake of  $26 \pm 2$  %ID/g at 144 hours[32], whereas the same mAb in humans with  
446 HNSCC had an average uptake of 19 %ID/kg[33]. From these data, it is apparent that uptake in  
447 man versus mouse is not directly scalable, but can depend on the mode of accumulation.  
448 Accordingly, we propose that if  $^{89}\text{Zr}$  localizes to tumors by transferrin binding and EPR uptake,  
449 the impact on proper assessment of tumor uptake may be greater in humans when imaging  
450 antibodies that primarily localize by active targeting.

451

452 Finally, turning to the pulmonary aspergillosis model, the results illustrate that when imaging  
453 animals with advanced disease, the presence of free  $^{89}\text{Zr}$  cannot be neglected. This disease  
454 model was expected to give an uptake of free  $^{89}\text{Zr}$  that was significantly different from naïve  
455 animals for several reasons. First, as the disease progresses the lung tissue becomes highly  
456 perfused, thereby giving a higher PET signal due to blood volume in the ROI, and due to EPR

457 localization. Second, the inflammation in the lungs would lead to an upregulation of the Tf-  
458 receptor causing accumulation of  $^{89}\text{Zr}$  that might have been associated with transferrin *in vivo*.  
459 And lastly, higher uptake was expected due to the presence of cyclic hydroxamate-based  
460 chelates in the extracellular environment of the fungus. The results of the present study do not  
461 weigh in on which of these probable causes are responsible, yet they do set a benchmark for  
462 significance when attempting targeted approaches to pulmonary aspergillosis imaging.

463

## 464 **5 Conclusions**

465

466 In this study we have shown that free  $^{89}\text{Zr}$ , in the form of  $^{89}\text{Zr}$  oxalate in saline, can exhibit  
467 substantial tumor accumulation as well as significant accumulation in *Aspergillus* infected lungs  
468 as compared to healthy lungs. Our results underline the importance of making sure that no free  
469  $^{89}\text{Zr}$  is present when conducting  $^{89}\text{Zr}$  PET imaging, especially in cancers and pulmonary  
470 aspergillosis, as observed accumulation of radioactivity may be non-specific. In addition, our  
471 results indicate that injection of free  $^{89}\text{Zr}$ , preferably as an oxalate at  $\text{pH} < 7$ , should routinely be  
472 performed as a control experiment to a preclinical study.

473

## 474 **6 Acknowledgements**

475



476 This research was supported by the EU grant FP7 MATHIAS project, the Danish Cancer Society,  
477 the Lundbeck Foundation, the Novo Nordisk Foundation, Innovationsfonden, the Svend  
478 Andersen Foundation and the Arvid Nilsson Foundation.

479

480 **7 References**

- 481 [1] Vugts DJ, Visser GWM, van Dongen GAMS.  $^{89}\text{Zr}$ -PET radiochemistry in the development  
482 and application of therapeutic monoclonal antibodies and other biologicals. *Curr Top*  
483 *Med Chem* 2013;13:446–57.
- 484 [2] Fischer G, Seibold U, Schirmacher R, Wängler B, Wängler C.  $^{89}\text{Zr}$ , a radiometal nuclide  
485 with high potential for molecular imaging with PET: chemistry, applications and  
486 remaining challenges. *Molecules* 2013;18:6469–90.
- 487 [3] Deri MA, Zeglis BM, Francesconi LC, Lewis JS. PET imaging with  $^{89}\text{Zr}$ : From radiochemistry  
488 to the clinic. *Nucl Med Biol* 2013;40:3–14.
- 489 [4] Zhang Y, Hong H, Cai W. PET tracers based on zirconium-89. *Curr Radiopharm*  
490 2011;4:131–9.
- 491 [5] Severin GW, Engle JW, Barnhart TE, Nickles RJ.  $^{89}\text{Zr}$  radiochemistry for positron emission  
492 tomography. *Med Chem* 2011;7:389–94.
- 493 [6] Chang AJ, Desilva R, Jain S, Lears K, Rogers B, Lapi S.  $^{89}\text{Zr}$ -radiolabeled trastuzumab  
494 imaging in orthotopic and metastatic breast tumors. *Pharmaceuticals* 2012;5:79–93.
- 495 [7] Van Rij CM, Sharkey RM, Goldenberg DM, Frielink C, Molkenboer JDM, Franssen GM, et  
496 al. Imaging of prostate cancer with immuno-PET and immuno-SPECT using a radiolabeled  
497 anti-EGP-1 monoclonal antibody. *J Nucl Med* 2011;52:1601–7.
- 498 [8] Holland JP, Divilov V, Bander NH, Smith-Jones PM, Larson SM, Lewis JS.  $^{89}\text{Zr}$ -DFO-J591 for  
499 immunoPET of prostate-specific membrane antigen expression in vivo. *J Nucl Med*  
500 2010;51:1293–300.
- 501 [9] Abou DS, Ku T, Smith-Jones PM. In vivo biodistribution and accumulation of  $^{89}\text{Zr}$  in mice.  
502 *Nucl Med Biol* 2011;38:675–81.
- 503 [10] Weiner R. The mechanism of  $^{67}\text{Ga}$  localization in malignant disease. *Nucl Med Biol*  
504 1996;23:745–51.
- 505 [11] Jørgensen JT, Persson M, Madsen J, Kjær A. High tumor uptake of  $^{64}\text{Cu}$ : implications for  
506 molecular imaging of tumor characteristics with copper-based PET tracers. *Nucl Med Biol*  
507 2013;40:345–50.
- 508 [12] Sotogaku N, Endo K, Hirunuma R, Enomoto S, Ambe S, Ambe F. Biochemical reactions of  
509 various trace elements with blood components and transport proteins. *J Radioanal Nucl*  
510 *Chem* 1999;239:429–32.

- 511 [13] Bal W, Sokołowska M, Kurowska E, Faller P. Binding of transition metal ions to albumin:  
512 sites, affinities and rates. *Biochim Biophys Acta* 2013;1830:5444–55.
- 513 [14] Heneweer C, Holland JP, Divilov V, Carlin S, Lewis JS. Magnitude of enhanced  
514 permeability and retention effect in tumors with different phenotypes: <sup>89</sup>Zr-albumin as a  
515 model system. *J Nucl Med* 2011;52:625–33.
- 516 [15] Matsumura Y, Maeda H. A new concept for macromolecular therapeutics in cancer  
517 chemotherapy: Mechanism of tumoritropic accumulation of proteins and the antitumor  
518 agent Smancs. *Cancer Res* 1986;46:6387–92.
- 519 [16] Schrettl M, Bignell E, Kragl C, Sabiha Y, Loss O, Eisendle M, et al. Distinct roles for intra-  
520 and extracellular siderophores during *Aspergillus fumigatus* infection. *PLoS Pathog*  
521 2007;3:1195–207.
- 522 [17] Petrik M, Haas H, Dobrozemsky G, Lass-Flörl C, Helbok A, Blatzer M, et al. <sup>68</sup>Ga-  
523 siderophores for PET imaging of invasive pulmonary aspergillosis: proof of principle. *J*  
524 *Nucl Med* 2010;51:639–45.
- 525 [18] Petrik M, Franssen GM, Haas H, Laverman P, Hörtnagl C, Schrettl M, et al. Preclinical  
526 evaluation of two <sup>68</sup>Ga-siderophores as potential radiopharmaceuticals for *Aspergillus*  
527 *fumigatus* infection imaging. *Eur J Nucl Med Mol Imaging* 2012;39:1175–83.
- 528 [19] Chiani M, Akbarzadeh A. Production of desferrioxamine B (Desferal) using corn steep  
529 liquor in *Streptomyces pilosus*. *Pak J Biol Sci* 2010;13:1151–5.
- 530 [20] Holland JP, Sheh Y, Lewis JS. Standardized methods for the production of high specific-  
531 activity zirconium-89. *Nucl Med Biol* 2009;36:729–39.
- 532 [21] Bruns S, Kniemeyer O, Hasenberg M, Amanianda V, Nietzsche S, Thywissen A, et al.  
533 Production of extracellular traps against *Aspergillus fumigatus* in vitro and in infected  
534 lung tissue is dependent on invading neutrophils and influenced by hydrophobin RodA.  
535 *PLoS Pathog* 2010;6:e1000873.
- 536 [22] Kobayashi T, Sasaki T, Takagi I, Moriyama H. Zirconium solubility in ternary aqueous  
537 system of Zr(IV)-OH-carboxylates. *J Nucl Sci Technol* 2009;46:142–8.
- 538 [23] Guérard F, Lee Y-S, Tripier R, Szajek LP, Deschamps JR, Brechbiel MW. Investigation of  
539 Zr(IV) and <sup>89</sup>Zr(IV) complexation with hydroxamates: Progress towards designing a better  
540 chelator than desferrioxamine B for immuno-PET imaging. *Chem Commun*  
541 2013;49:1002–4.
- 542 [24] Holland JP, Evans MJ, Rice SL, Wongvipat J, Sawyers CL, Lewis JS. Annotating MYC status  
543 with <sup>89</sup>Zr-transferrin imaging. *Nat Med* 2012;18:1586–91.

- 544 [25] Gotthardt M, Bleeker-Rovers CP, Boerman OC, Oyen WJG. Imaging of inflammation by  
545 PET, conventional scintigraphy, and other imaging techniques. *J Nucl Med Technol*  
546 2013;41:157–69.
- 547 [26] Vavere AL, Welch MJ. Preparation, biodistribution, and small animal PET of <sup>45</sup>Ti-  
548 transferrin. *J Nucl Med* 2005;46:683–90.
- 549 [27] Jensen AI, Binderup T, Kumar EK P, Kjær A, Rasmussen PH, Andresen TL. Positron  
550 emission tomography based analysis of long-circulating cross-linked triblock polymeric  
551 micelles in a U87MG mouse xenograft model and comparison of DOTA and CB-TE2A as  
552 chelators of copper-64. *Biomacromolecules* 2014;15:1625–33.
- 553 [28] Petersen AL, Binderup T, Rasmussen P, Henriksen JR, Elema DR, Kjær A, et al. <sup>64</sup>Cu loaded  
554 liposomes as positron emission tomography imaging agents. *Biomaterials* 2011;32:2334–  
555 41.
- 556 [29] Abou DS, Thorek DLJ, Ramos NN, Pinkse MWH, Wolterbeek HT, Carlin SD, et al. <sup>89</sup>Zr-  
557 labeled paramagnetic octreotide-liposomes for PET-MR imaging of cancer. *Pharm Res*  
558 2013;30:878–88.
- 559 [30] Harrington KJ, Syrigos KN, Uster PS, Abra RM, Stewart JSW. Biodistribution and  
560 pharmacokinetics of In-DTPA-labelled pegylated liposomes in a human tumour xenograft  
561 model : implications for novel targeting strategies. *Br J Cancer* 2000;83:232–8.
- 562 [31] Harrington KJ, Mohammadtaghi S, Uster PS, Harrington KJ, Mohammadtaghi S, Uster PS,  
563 et al. Effective targeting of solid tumors in patients with locally advanced cancers by  
564 radiolabeled pegylated liposomes effective targeting of solid tumors in patients with  
565 locally advanced cancers by radiolabeled pegylated liposomes. *Clin Cancer Res*  
566 2001:243–54.
- 567 [32] Verel I, Visser GWM, van Dongen GAMS. The promise of immuno-PET in  
568 radioimmunotherapy. *J Nucl Med* 2005;46 Suppl 1:164S–71S.
- 569 [33] Börjesson PKE, Jauw YWS, de Bree R, Roos JC, Castelijns JA, Leemans CR, et al. Radiation  
570 dosimetry of <sup>89</sup>Zr-labeled chimeric monoclonal antibody U36 as used for immuno-PET in  
571 head and neck cancer patients. *J Nucl Med* 2009;50:1828–36.

572

573

574 **Table 1.** pH ranges of  $^{89}\text{Zr}$  complex preparations as measured after 10 minutes of mixing of  $^{89}\text{Zr}$   
 575 chloride with the corresponding solution.

Mixture	pH range
Oxalate 5.5	4.87 – 6.01
Oxalate 7.0	6.74 – 7.45
Citrate 5.5	5.43 – 5.58
Citrate 7.0	6.60 – 6.93
Sucrose	5.12 – 6.77
Acetate 5.5	5.51 – 5.52
Acetate 7.0	6.43 – 7.54
Chloride	4.99 – 5.68
Water	4.65 – 4.95

576

577

578 **Table 2.** Biodistribution of  $^{89}\text{Zr}$ , injected as the oxalate, in tumor-bearing mice. Averages and  
 579 standard deviations are given (n = 3 for FaDu, n = 4 for HT29). Animals were injected  
 580 intravenously with  $^{89}\text{Zr}$  oxalate and imaged for up to 68 h. Tumor levels were higher than muscle  
 581 at all measurement points. Tumor levels were higher than blood (heart) after 45 h. Errors indicate  
 582 one standard deviation. 9-15 MBq was administered to each mouse, 10 min scans were acquired

		%ID/g ( $\pm$ SD)						
	Xenograft	Heart	Kidney	Bladder	Liver	Tumor	Muscle	Bone
	<b>All (n = 7)</b>	<b>10.59 (<math>\pm</math> 2.47)</b>	<b>4.69 (<math>\pm</math> 1.21)</b>	<b>4.04 (<math>\pm</math> 2.91)</b>	<b>6.07 (<math>\pm</math> 1.92)</b>	<b>2.99 (<math>\pm</math> 0.35)</b>	<b>1.98 (<math>\pm</math> 0.31)</b>	<b>4.30 (<math>\pm</math> 1.08)</b>
<b>1h</b>	FaDu	11.83 ( $\pm$ 3.01)	5.55 ( $\pm$ 1.45)	2.93 ( $\pm$ 1.00)	7.40 ( $\pm$ 2.26)	2.97 ( $\pm$ 0.37)	2.03 ( $\pm$ 0.42)	4.53 ( $\pm$ 1.66)
	HT29	9.65 ( $\pm$ 1.84)	4.05 ( $\pm$ 0.48)	4.88( $\pm$ 3.76)	5.08 ( $\pm$ 0.93)	3.00 ( $\pm$ 0.36)	1.94 ( $\pm$ 0.26)	4.13 ( $\pm$ 0.64)

	<b>All (n = 7)</b>	<b>5.31 (± 2.42)</b>	<b>2.56 (± 1.09)</b>	<b>3.26 (± 0.91)</b>	<b>3.36 (± 1.69)</b>	<b>3.46 (± 0.65)</b>	<b>1.76 (± 0.46)</b>	<b>9.04 (± 2.59)</b>
<b>6h</b>	FaDu	6.53 (± 2.95)	3.25 (± 1.31)	3.23 (± 1.46)	4.37 (± 2.02)	4.08 (± 0.41)	2.05 (± 0.55)	10.37 (± 3.58)
	HT29	4.40 (± 1.81)	2.04 (± 0.61)	3.28 (± 0.48)	2.60 (± 1.09)	2.99 (± 0.29)	1.54 (± 0.25)	8.05 (± 1.35)
	<b>All (n = 7)</b>	<b>1.86 (± 1.49)</b>	<b>1.35 (± 0.68)</b>	<b>1.05 (± 0.28)</b>	<b>1.77 (± 1.33)</b>	<b>2.99 (± 1.22)</b>	<b>0.99 (± 0.40)</b>	<b>12.76 (± 2.24)</b>
<b>20h</b>	FaDu	3.07 (± 1.47)	1.85 (± 0.77)	1.15 (± 0.34)	2.77 (± 1.46)	4.13 (± 0.96)	1.37 (± 0.23)	13.63 (± 1.56)
	HT29	0.95 (± 0.65)	0.97 (± 0.31)	0.97 (± 0.25)	1.03 (± 0.60)	2.14 (± 0.40)	0.71 (± 0.18)	12.10 (± 2.65)
	<b>All (n = 7)</b>	<b>0.67 (± 0.56)</b>	<b>0.91 (± 0.44)</b>	<b>0.60 (± 0.22)</b>	<b>1.39 (± 0.99)</b>	<b>2.47 (± 0.95)</b>	<b>0.76 (± 0.36)</b>	<b>14.89 (± 1.32)</b>
<b>45h</b>	FaDu	1.09 (± 0.67)	1.24 (± 0.53)	0.72 (± 0.32)	2.14 (± 1.19)	3.27 (± 0.97)	1.07 (± 0.36)	13.17 (± 0.78)
	HT29	0.35 (± 0.09)	0.66 (± 0.10)	0.50 (± 0.04)	0.83 (± 0.26)	1.88 (± 0.23)	0.53 (± 0.10)	15.58 (± 1.25)
	<b>All (n = 7)</b>	<b>0.55 (± 0.31)</b>	<b>0.86 (± 0.32)</b>	<b>0.50 (± 0.08)</b>	<b>1.30 (± 0.82)</b>	<b>2.05 (± 0.76)</b>	<b>0.65 (± 0.29)</b>	<b>12.99 (± 1.45)</b>
<b>68h</b>	FaDu	0.86 (± 0.14)	1.00 (± 0.40)	0.54 (± 0.08)	1.93 (± 0.92)	2.72 (± 0.74)	0.78 (± 0.37)	13.77 (± 0.32)
	HT29	0.32 (± 0.06)	0.75 (± 0.24)	0.48 (± 0.07)	0.82 (± 0.27)	1.55 (± 0.13)	0.56 (± 0.20)	12.41 (± 1.75)

583

584

585

586 **Table 3.** *Ex vivo* biodistribution of organs of naïve (n = 4) and infected mice (n = 4). The mice  
587 were infected with *A. fumigatus* and after 21 hours of disease progression, they were injected  
588 with 10-12 MBq <sup>89</sup>Zr oxalate. Tissues were excised and measured three hours after the injection.  
589 Data are %ID/g, expressed as the mean or as lung-to-muscle ratios ± 1 SD. Significantly  
590 different organs are shown in bold with \* (p < 0.05) or \*\* (p < 0.01).

Organ	Naïve mice	Infected mice
Blood	10.5 (± 2.7)	8.6 (± 2.8)
<b>Lung**</b>	<b>6.0 (± 1.1)</b>	<b>11.6 (± 1.8)</b>
Muscle	1.6 (± 0.5)	1.9 (± 0.2)
Liver	4.0 (± 0.8)	3.3 (± 0.7)
Heart	5.8 (± 2.2)	5.6 (± 1.5)
Kidney	6.1 (± 1.5)	8.3 (± 1.6)

<b>Stomach*</b>	<b>2.5 (± 0.2)</b>	<b>3.5 (± 0.7)</b>
<b>Colon*</b>	<b>2.6 (± 0.4)</b>	<b>3.5 (± 0.2)</b>
Brain	0.5 (± 0.1)	0.5 (± 0.1)
<b>Spine*</b>	<b>5.0 (± 0.9)</b>	<b>3.8 (± 0.4)</b>
Femur right	9.9 (± 4.3)	6.6 (± 0.5)
Femur left	9.0 (± 3.5)	6.5 (± 1.3)
Lung/muscle	3.8 (± 2.3)	6.3 (± 7.7)

---

591

592

593

594

595

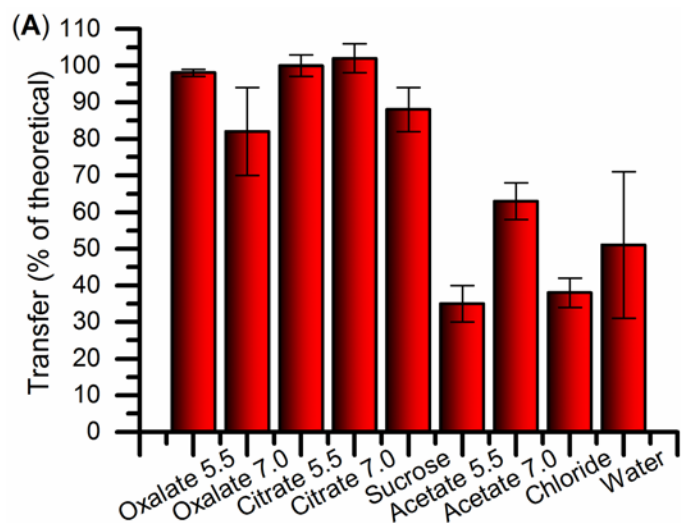
596

597

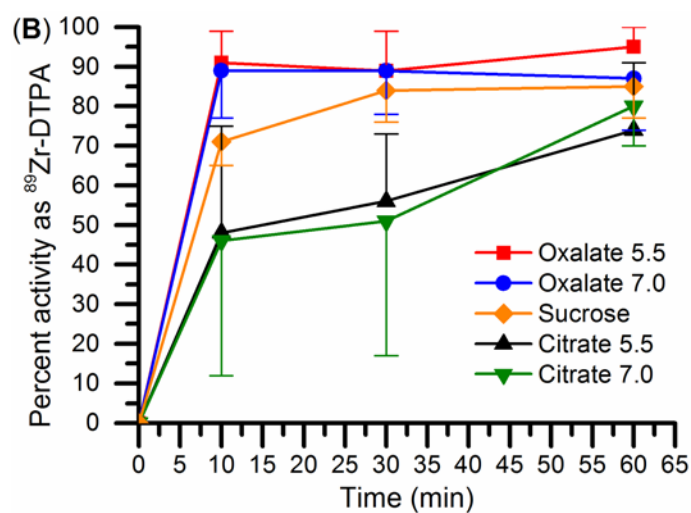
598

599

600



601

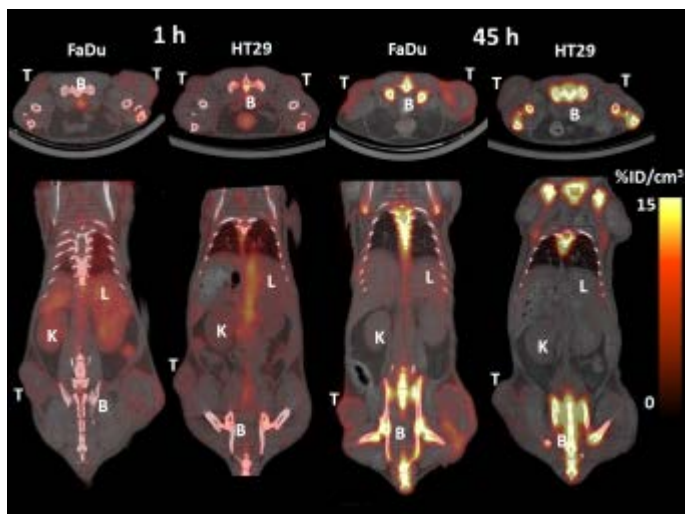


602

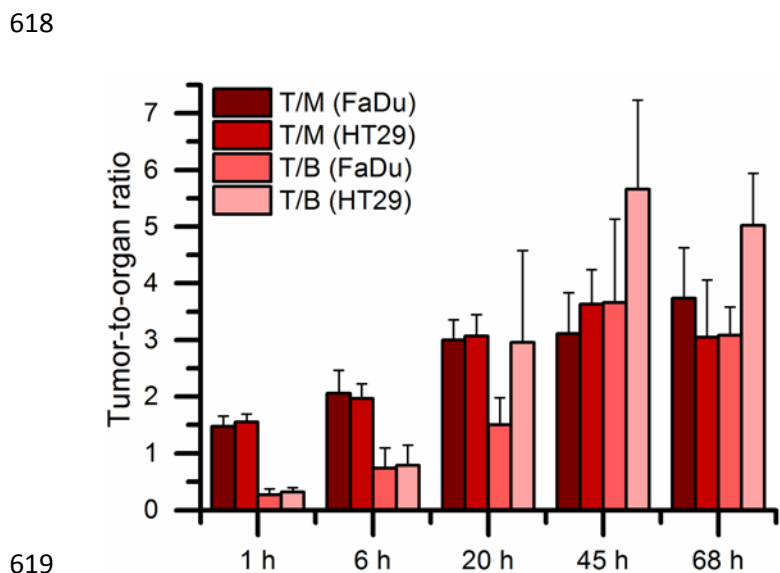
603 **Figure 1.** (A) Transferability/dissolution of <sup>89</sup>Zr mixtures. The y-axis shows transferability as the  
 604 activity in a removed aliquot of 300  $\mu$ L compared to the theoretical maximum activity removed  
 605 from a homogeneous solution, as calculated by the equation  $transferability = A_{300\mu L} * (1.3/0.3) /$   
 606  $A_{1300\mu L} * 100\%$ . n = 3 in all cases, error bars show one standard deviation. (B) Transchelation of  
 607 <sup>89</sup>Zr mixtures to DTPA. Oxalate at both pH values showed fast transchelation, reaching about  
 608 90% after 10 minutes, while sucrose and especially the citrates showed a slower shift of the  
 609 radioactivity to DTPA. n = 3 in all cases, error bars showing one standard deviation are one-  
 610 sided to improve legibility.

611



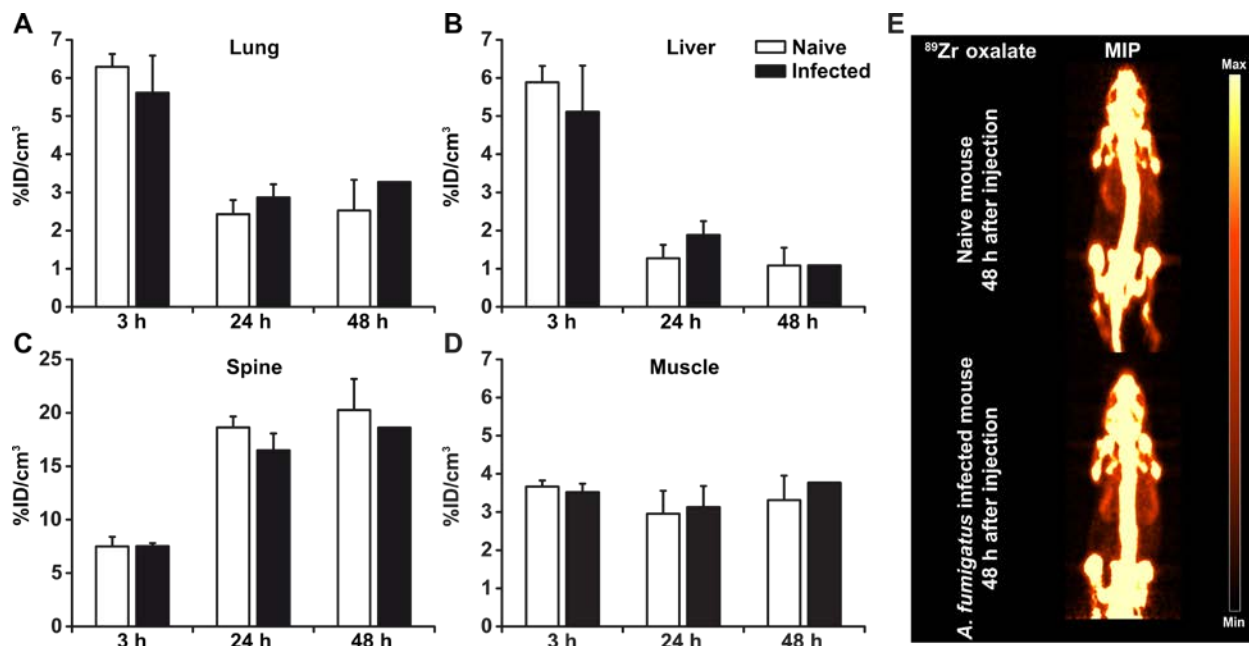


612  
 613 **Figure 2.** Representative transverse (top lane) and coronal (bottom lane) images of  $^{89}\text{Zr}$ -  
 614 distribution in FaDu and HT29 tumor bearing animals acquired by ten minute static PET scans, 1  
 615 h (left) and 45 h (right) after tracer administration (FaDu: 12.47 MBq injected, HT29: 9.40 MBq  
 616 injected). Animals were sedated with sevoflurane. White letters on images marks T: tumor; B:  
 617 bone; L: liver and K: kidney.

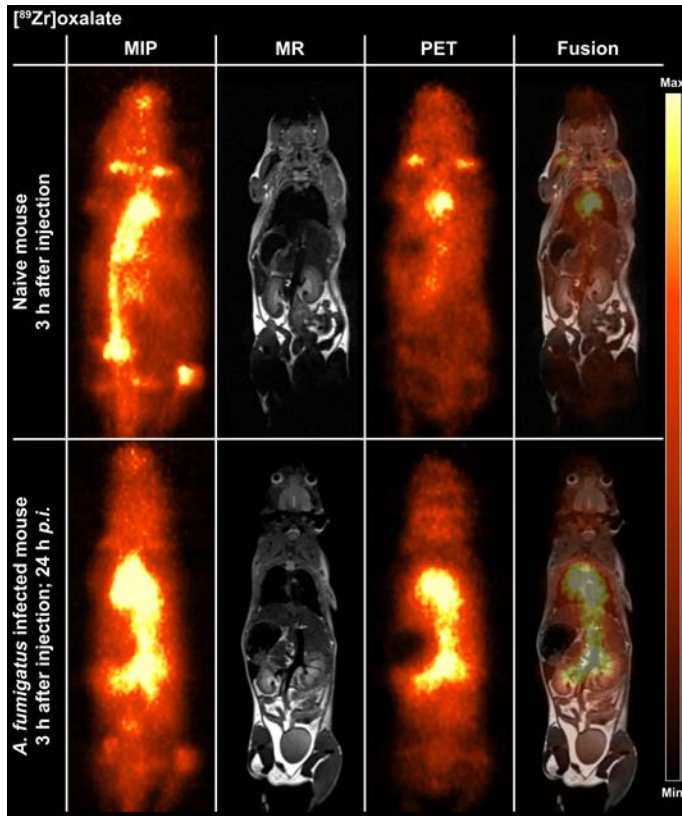


619  
 620 **Figure 3.** Tumor-to-muscle (T/M) and tumor-to-blood (T/B) ratios of injected  $^{89}\text{Zr}$  oxalate in  
 621 mice bearing FaDu or HT29 tumor xenografts. The blood values are taken as  $\%ID/cm^3$  of the  
 622 heart. The T/M values for both tumor types are seen to rise until 20 h and subsequently stabilize

623 between 3.0-3.7 for both tumors. T/B values for both tumor types increase until 45 h. Error bars  
 624 indicate one standard deviation. n = 3 (FaDu), n = 4 (HT29). 9-15 MBq was administered to each  
 625 mouse, 10 min scans were acquired.  
 626

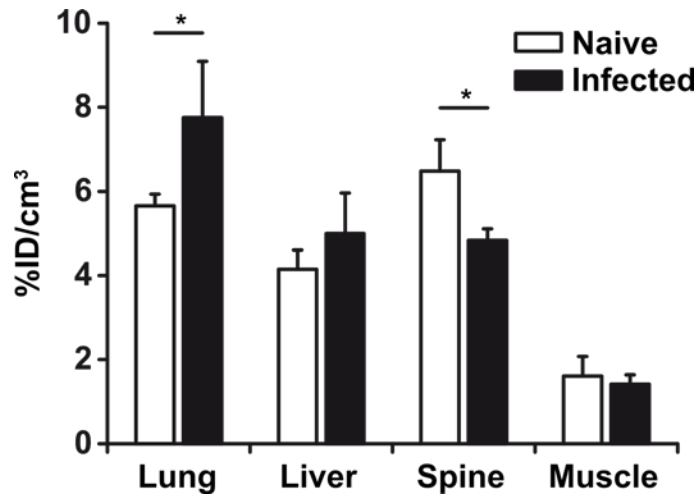


627  
 628 **Figure 4 (A)-(D).** PET quantification (%ID/cm<sup>3</sup>) of organs of naïve and infected mice 3 h, 24 h,  
 629 48 h post injection of <sup>89</sup>Zr oxalate. (E) Maximum intensity projection (MIP) of a naïve and an  
 630 infected mouse at the 48 h time-point, demonstrating the high uptake of <sup>89</sup>Zr in the bones.  
 631 Injected radioactivity was between 10 and 12 MBq. The mice were sedated with isoflurane and  
 632 scanned for 10 minutes. Data are given as %ID/cm<sup>3</sup> ± 1 SD.



633

634 **Figure 5.** Maximum intensity projections (MIP) of PET and fused PET and MR images of naïve  
 635 or neutropenic *A. fumigatus* infected mice. The PET/MR imaging was done three hours after  
 636 injection with  $^{89}\text{Zr}$  oxalate and 21 hours post infection (p.i.) of the mice with *A. fumigatus*.  
 637 Perfusion effects and thereby enhanced  $^{89}\text{Zr}$  oxalate accumulation is seen in the lungs of the *A.*  
 638 *fumigatus* infected mouse as depicted in the lower lane. The mice were sedated with isoflurane  
 639 and scanned for 10 minutes. Injected radioactivity was between 10 and 12 MBq



640

641 **Figure 6.** PET quantification (%ID/cm<sup>3</sup>) of tissue ROIs from naïve and infected mice with  
 642 advanced disease. The data were taken 24 h post-infection, and 3 h after injection of <sup>89</sup>Zr oxalate.

643 Data are given as %ID/cm<sup>3</sup> ± 1 SD. \*Tissues are considered statistically significant, with p<0.05.

644

645